Power Electronics Research and Development Laboratory
Vancouver, Canada

Proceedings of Annual IEEE Conference on Applied Power Electronics Conference and Exposition (APEC), San Antonio, Texas, March 22 – 26, 2026.

Seamless Power Transfer of Bidirectional Converters in Microgrids Applications

E. Serban,
C. Lascu

Seamless Power Transfer of Bidirectional Converters in Microgrids Applications

Emanuel Serban
Hillcrest Energy Technologies Ltd
R&D Engineering
Vancouver, Canada
eserban@hillcrestenergy.tech

Cristian Lascu
Department of Electrical Engineering
University POLITEHNICA Timişoara
Timisoara, Romania
cristian.lascu@ upt.ro

Abstract - **Power converters utilizing bidirectional topologies are essential for maintaining continuous microgrid operation and ensuring reliable power delivery to both DC and AC loads. This paper introduces a hybrid AC–DC microgrid architecture that delivers reliable power to various loads while providing enhanced operational flexibility and robust resilience under dynamic and fault conditions. The design and inclusion of a bidirectional DC-DC converter provides critical functionalities such as prioritization of essential loads (e.g., life-support systems), extension of the DC voltage operating range, and galvanic isolation.**

During dynamic microgrid's operating conditions, the high-frequency transformer within the DC–DC converter can exhibit increased sensitivity to pulsewidth modulation (PWM) mismatches, saturation and delayed response in power transfer detection. To address these challenges, a microgrid controller is proposed and integrated within the DC–DC converter to enable seamless power transfer during charge and discharge transitions. The proposed communication-free control strategy employs a voltage gradient detection method for rapid event identification and smooth bidirectional power transfer. Each module within the DC microgrid autonomously monitors local parameters and, based on positive or negative voltage gradient variations, determines its operating mode accordingly. The effectiveness of the proposed strategy is validated through experimental laboratory studies conducted under dynamic charging and discharging scenarios.

Keywords— Hybrid AC-DC microgrids, DC microgrids, seamless power transfer, phase-shift control.

I. INTRODUCTION

Emerging applications such as electric vehicle chargers, data centers, medical life support systems and solar photovoltaic systems demand the integration of advanced power electronic topologies and control strategies with energy storage systems [1], [2], [3], [4].

The energy storage systems require fast switchover between sources and loads, while maintaining both AC and DC microgrids. AC-DC microgrids have been investigated to achieve switching transitions between islanded and grid-connected operation modes, by implementing droop and PQ control verified with simulation tools [5], [6], [7], [8]. Bidirectional DC-DC buck-boost converters have been used in DC microgrids studies, to demonstrate voltage regulation, system stability and energy management [9], [10], [11]. In order to achieve higher conversion ratios, extend the operational voltage range, and enhance the resilience of DC microgrids, isolated bidirectional DC-DC converter topologies have demonstrated to be effective and viable solutions [12], [13]. Communication-free power management control with seamless hot-swap for DC microgrid regulation has been implemented with droop control using dual-active bridge (DAB) converters in [14]. However, the hardware platform is using two DAB converters running at reduced power, voltage levels and switching frequency. Simulation platforms have been used for DC microgrids with solar PV and battery energy storage, using step-down and step-up converters for seamless transitions under sudden load changes in [15]. DC microgrids have been investigated, with parallel bidirectional power converters with DC power sharing, using $V^2 - P$ droop control with constant power loads connected to DC microgrids, using hardware-in-the-loop simulation tools [16], [17].

DC microgrid with distributed energy resources (DER) in DC distribution, data centers, residential and commercial remote systems, require continuous operation without load power interruptions during grid failures. Local power-based droop controller for DER in DC microgrids has been implemented for seamless transitions between grid-interface converter and DC-DC converters for bus voltage regulation [18]. However, in [18] a microgrid architecture has been experimentally tested using half-bridge buck-type hardware power converters platforms.

This article proposes a hybrid microgrid system architecture capable of delivering seamless, uninterrupted power to critical loads during AC grid failures or disturbances. The main contributions of this research are:

1) The proposed hybrid AC–DC microgrid architecture incorporates both grid-following (GFL) and grid-forming (GFM) operational modes and seamlessly integrates distributed energy resources with diverse load types. On the AC side, a four-leg inverter interfaces with the utility grid to deliver backup power to AC loads [20], [21], [22], [23], [24]. On the DC side, a dual-active-bridge (DAB) converter with a reconfigurable output stage supplies power to critical DC loads. The converter's flexible voltage extension is enabled through a parallel-series bridge reconfiguration scheme. An energy storage system is additionally integrated to enhance the reliability of essential load supply and to ensure continuous backup operation during AC grid interruptions.

2) A microgrid control framework enabling seamless transitions between operating modes is developed. AC grid failure is detected without communication links by employing voltage-region identification. On the DC side, grid-failure detection is achieved by monitoring the voltage gradient of the DC microgrid. This method supports seamless bidirectional power transfer during both disconnecting and reconnection events, facilitated by an automatic recovery control mechanism. The proposed DC microgrid voltage-based region strategy effectively minimizes transient deviations; both undershoot and overshoot, as demonstrated experimentally on a 6 kW prototype platform.

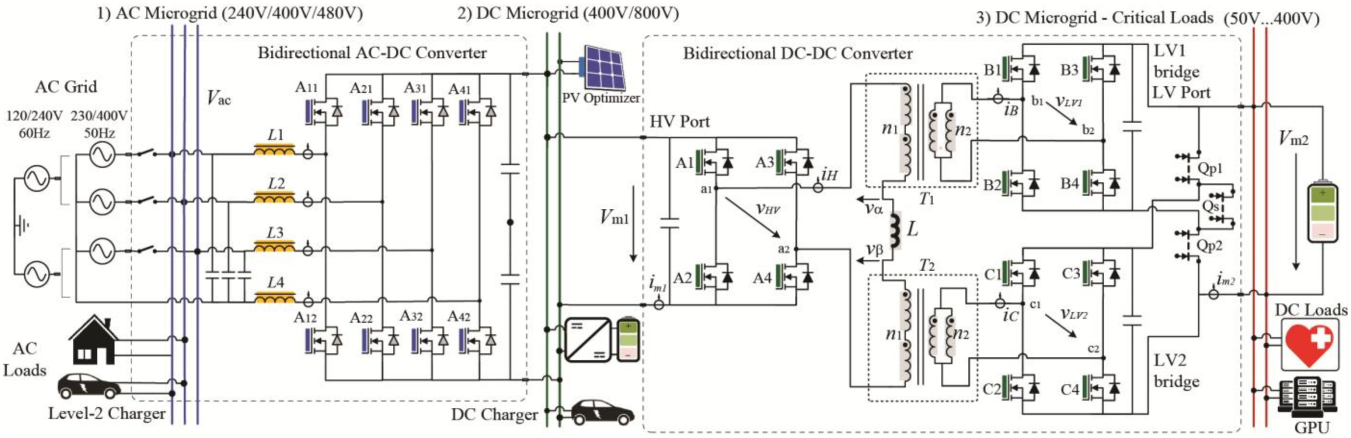

Fig. 1. Microgrid architecture with AC-DC and DC-DC converters for continuous load supply: a) AC microgrid, DC microgrid and DC microgrid for critical loads.

The proposed hybrid AC-DC microgrid architecture is described in Section II. The DC microgrid voltage-current control scheme, including the bidirectional power flow control strategy, is presented in Sections III and IV. Section V provides experimental verification and validation of the overall system, followed by concluding remarks and research perspectives in Section VI.

II. MICROGRID SYSTEM DESCRIPTION

DC microgrids are increasingly preferred for DER applications due to their ability to improve overall system efficiency. Fig. 1 shows the proposed hybrid AC/DC microgrid architecture, consisting of three interconnected microgrids.

1) *AC microgrid:* employs a bidirectional AC-DC inverter capable of both GFM and GFL operation. The inverter features a four-leg topology that supports both single-phase and three-phase system applications. For 120/240V-60 Hz split-phase operation, two legs ($A_{11}-A_{12}$ and $A_{21}-A_{22}$) are paralleled to form one phase, while the remaining two legs ($A_{31}-A_{32}$ and $A_{41}-A_{42}$) are paralleled to form the second phase, with the two groups operated 180° out of phase. For three-phase operation (e.g., 400V-50 Hz or 480V-60 Hz), the neutral leg ($A_{41}-A_{42}$) is utilized in GFM mode to provide current balancing and support unbalanced load conditions.

In GFL mode, the inverter draws power from the AC grid while regulating the DC microgrid voltage V_{m1}. When surplus power is available from the solar DC optimizers within the DC microgrid, the GFL inverter exports the excess energy back to the AC grid.

During power outage conditions, the AC relays disconnect the system from the grid, and the inverter transitions to GFM mode to supply and regulate the AC microgrid autonomously.

2) *DC microgrid for essential loads:* supplies distributed loads such as lighting, EV chargers, and other auxiliary systems. It also interfaces with renewable energy sources, providing additional support to the overall hybrid microgrid. The nominal operating voltage in this work is $v_{m1} = 400$ V, although the architecture can be readily extended to 800 V.

3) *DC microgrid for critical loads:* delivers uninterrupted power to critical systems, including life-support equipment, security infrastructure, and high-performance graphical processing units (GPUs) used in AI-driven applications. The critical loads voltage can be configured in the range of $v_{m2} =$ 50 to 400 V.

In this article, the DAB-based bidirectional DC-DC converter includes a high-voltage (HV) bridge, and two low-voltage (LV) bridges, LV1 and LV2, which can be configured in parallel operation through switches Q_{p1} and Q_{p2}. For higher-voltage operation, the two bridges may be series-connected via switch Q_s. The bidirectional DC-DC converter constitutes a central component of the overall microgrid architecture shown in Fig. 1 and is the subject of detailed analysis in this study.

The architecture presented in Fig. 1 is inherently scalable, allowing multiple AC-DC inverters and DC-DC converters to operate in parallel to increase system capacity and functionality. For instance, expanding the DC microgrid distribution within data centers can replace conventional AC uninterruptible power supply (AC-UPS) systems, as illustrated in Fig. 1. The HV windings of T_1 and T_2 are connected in series, as illustrated in Fig. 1. The inductor, positioned between the series-connected secondaries and the HV bridge, plays a critical role in regulating the bidirectional power flow. From Fig. 1, the voltage superimposed on L can be expressed as per (1).

$$v_L(t) = L\frac{d}{dt}i_H(t) = v_\alpha(t) - v_\beta(t) \tag{1}$$

The inductor current i_H on the HV side can be calculated by

$$i_H(t) = i_H(t_0) + \frac{1}{\mathrm{L}}\int_{t_0}^{t_1} v_L(\mathrm{t}). \tag{2}$$

where $i_H(t_0)$ is the current at the initial moment t_0 and t_1 denotes the final moment of inductor current. The instantaneous power delivered in charge or discharge mode by $v_\alpha(t)$ and $v_\beta(t)$ can be expressed as the product of instantaneous voltage and current as shown in

$$\begin{cases} p_\alpha(t) = v_\alpha(t) i_{\mathrm{H}}(\mathrm{t}) \\ p_\beta(t) = v_\beta(t) i_{\mathrm{H}}(\mathrm{t}). \end{cases} \tag{3}$$

The average active power P_α and P_β generation during one switching period (T) can be derived as per equation,

$$\begin{cases} P_\alpha = \frac{1}{T}\int_{t_0}^{t_1} v_\alpha(t) i_{\mathrm{H}}(\mathrm{t})\, dt \\ P_\beta = \frac{1}{T}\int_{t_0}^{t_1} v_\beta(t) i_{\mathrm{H}}(\mathrm{t})\, dt. \end{cases} \tag{4}$$

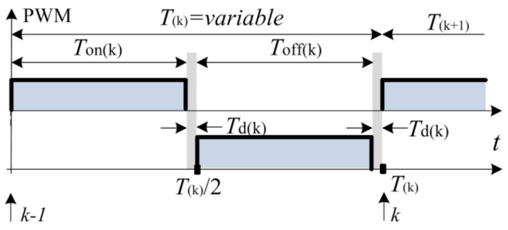

Fig. 2. PWM signal generation for complementary switch pairs within a single channel PWM generator.

Fig. 2 shows the PWM generation for complementary DAB switches, with cycle-by-cycle calculation and update for period and dead time, which ensures mitigation of the DC offsets. As can be noted, both period and dead time are variable during converter operation. The period calculation must satisfy (5) at the moment of the switching period (k).

$$\begin{cases} T_{(k)} = T_{on(k)} + T_{off(k)} + 2T_{d(k)} \\ T_{on(k)} = T_{off(k)} \end{cases} \tag{5}$$

$$T_{(k)}/2 = T_{o(k)} + T_{d(k)} \tag{6}$$

The attainable resolution of the phase setting is determined by the internal digital clock period (T_{clk}) of the DSP. A single clock period represents the minimum phase adjustment step size, corresponding to a phase angle resolution of $(\delta, \alpha, \beta)_{res}$ as per

$$\begin{cases} T_{clk} = \frac{1}{f_{clk}} \\ (\delta, \alpha, \beta)_{res} = 2\pi \frac{T_{clk}}{T} \end{cases} \tag{7}$$

The bidirectional power flow between the source and the load is regulated by the phase shift δ. As illustrated in Fig. 1, the HV-bridge voltage v_{HV} leads v_{LV} determining the power transfer from the HV bus to LV critical load port. During dynamic phase transitions, the on/off durations, dead time, and consequently the overall PWM period may change in order to satisfy the required timing relationship (6). When the desired voltage/current set-points change, the DSP updates the phase angles (α, β, δ) and recalculates $T_{on(k)}, T_{off(k)}$ and $T_{d(k)}$ for the next switching cycle, using (5) and (6). Under these operating conditions, the proposed method ensures PWM symmetry by adaptively adjusting both the period and the dead time, thereby preventing DC offsets and ultimately avoiding transformer saturation.

III. Current and Voltage Controllers For DC Microgrid System

Fig. 3 illustrates the design and implementation of the control strategy for the DC-DC converter. The main controller is responsible for generating the reference set-points required for bidirectional operation. During discharge mode, the controller sets the voltage and current references as v_{m1}^* and i_{m1}^*, respectively, to regulate the power delivery from LV side. In charge mode, the voltage and current references are defined as v_{m2}^* and i_{m2}^*, respectively, to control the power flow toward the LV battery port. This control framework will enable seamless transitions between operating modes while ensuring stable and efficient power conversion. The current and voltage controllers are implemented using proportional-integral (PI) control:

$$G_i(s) = K_{Pi} + K_{Ii}\frac{1}{s} \tag{8}$$

$$G_v(s) = K_{Pv} + K_{Iv}\frac{1}{s} \tag{9}$$

where $K_{Pi}, K_{Ii}, K_{Pv}, K_{Iv}$ are constant gains and s is the Laplace operator. The controllers are arranged in a cascaded configuration, with the current controller forming the inner loop and the voltage controller the outer loop. The control variable of the system is the outer phase shift δ between the HV and LV bridges.

The open-loop model of a DAB, with i_{m2} current as output and δ as input, can be approximated by second-order or first-order transfer functions [19]. We assume a simple first-order model $B_{i2}(s) = i_{m2}/\delta = K/(sT_e + 1)$. The time constant is roughly estimated as $T_e = L/R_{eq}$ where R_{eq} is an equivalent lumped resistance that accounts for copper losses in inductor and transformers, for MOSFET conduction losses and for load resistances. With this model, and using controller (8), the closed-loop transfer function of the current control loop is:

$$H_{i2}(s) = \frac{i_{m2}(s)}{i_{m2}^*(s)} = \frac{K(K_{Pi}s + K_{Ii})}{s^2T + (KK_{Pi} + 1)s + KK_{Ii}} \tag{10}$$

This system is stable for positive gains, $K, K_{Pi}, K_{Ii} > 0$.

To analyze the voltage loop, we take into account the open-loop model of a capacitor $C_v(s) = v_{m2}/i_c = 1/Cs$. Assuming fast and accurate current control, $i_{m2} = i_{m2}^*$, the closed-loop transfer function of the output voltage, v_{m2} control loop is:

$$H_{v2}(s) = \frac{v_{m2}(s)}{v_{m2}^*(s)} = \frac{K_{Pv}s + K_{Iv}}{s^2C + K_{Pv}s + K_{Iv}} \tag{11}$$

which is stable for positive gains, $K_{Pv}, K_{Iv} > 0$.

A similar transfer function can be obtained for discharging operation, by substituting v_{m1} for v_{m2} in (11).

The cascade architecture allows charging batteries in both constant current or constant voltage modes. In order to charge at constant current, the reference voltage v_{m2}^* is set equal to the maximum battery voltage, which is larger than the actual battery voltage. In this case, the voltage controller saturates the reference current at the maximum charging current, and thus the charging current is constant. As the battery charges, its voltage approaches and reaches the maximum voltage, the voltage controller becomes active and then the battery is charged in constant voltage mode.

The AC-DC grid converter is controlled by a conventional cascaded scheme. In charging mode, PI current controllers implemented in the synchronous $d-q$ rotating reference frame regulate the grid currents, while a single PI controller governs the DC-link voltage [20], [22]. In discharging mode, the converter operates in grid-forming mode using a similar cascaded arrangement, with $d-q$ current controllers, employed along with two additional PI voltage controllers to regulate the AC grid voltages. Alternatively, a direct AC voltage control strategy may be adopted for grid-voltage regulation, as demonstrated in [21].

The voltage and current controllers, $G_v(s)$ and $G_i(s)$, regulate the outer phase shift δ between the HV bridge and the LV bridges to control power transfer from the source to the load. The inner phase-shifts α and β are employed to extend the soft-switching range, thereby enhancing the conversion efficiency.

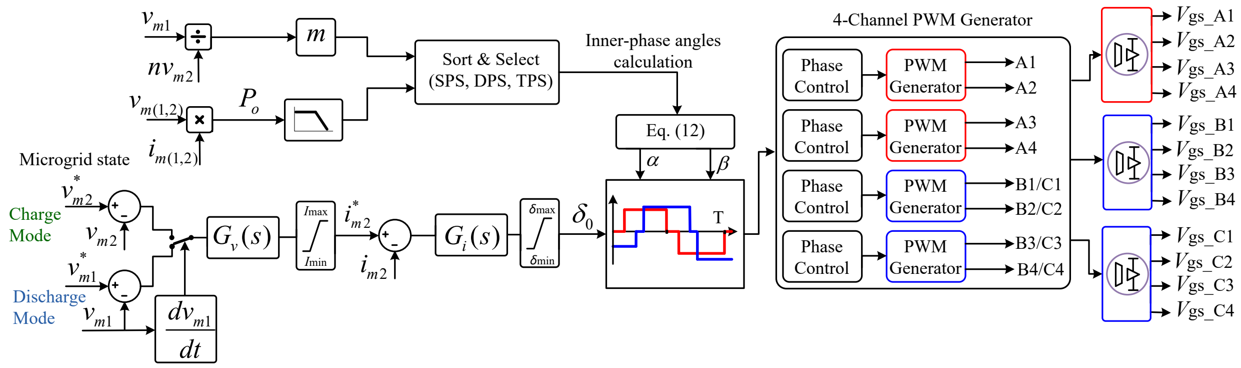

Fig. 3. Proposed control strategy of bidirectional DC-DC converters for microgrid applications.

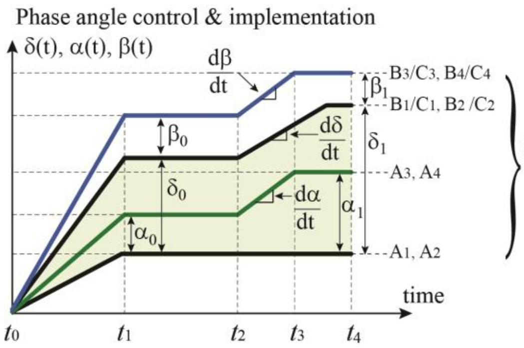

Fig. 4. Design and operation example of phase angles control.

The phase angles of the four legs of the DAB converter are shown on Fig. 4, which shows an example when the phase angles transition between switching states. On interval $t_1 - t_2$, the control of switches A_3, A_4 lags that of A_1, A_2 which generate the inner phase, with an initial value α_0. The inner phase for LV-bridges is determined by the angle between B_1, B_2 and B_3, B_4 with an initial value β_0. The phase shift between HV-bridge and LV-bridge determines the power flow through the phase shift from an initial value δ_0 and the outer phase angle δ is

$$\begin{cases} \delta = \delta_0 + \frac{\alpha-\beta}{2}, |\delta| \in \left[0, \frac{\pi}{2}\right] \\ \frac{d\alpha}{dt} < \frac{\Delta\alpha_{lim}}{T} \\ \frac{d\beta}{dt} < \frac{\Delta\beta_{lim}}{T} \end{cases} \quad (12)$$

where the slope limits $\Delta\alpha_{\text{lim}}$, $\Delta\beta_{\text{lim}}$, are predefined constant values for the inner angles. The active power monotonically increases with phase angle δ,

$$P = nV_{m1}V_{m2}\frac{\delta(\pi-|\delta|)}{2\pi^2 fL} = \frac{nV_{m1}V_{m2}}{2\pi fL}\delta\left(1-\frac{|\delta|}{\pi}\right). \quad (13)$$

where L is the converter inductance operating at switching frequency f, and $n = (2n_1)/n_2$ is the total ratio of galvanic isolation of the DAB converter.

IV. Voltage-Based Control for Seamless Power Flow Transfers

Fig. 5 shows the simplified hybrid microgrid using a grid-connected AC-DC inverter and the bidirectional DC-DC converter for battery charge and discharge for grid and load support. The DC bus voltage is monitored to enable automatic charge-discharge decision-making transfer. In charge mode from the grid, if the DC bus voltage drops, indicating a potential grid outage, the controller switches to discharge mode. In this scenario, the battery supplies the necessary power to support all DC loads.

Fig. 6 shows the detection method for fast charge-discharge transfer. The charging-discharging controller operates as a binary decision unit that continuously monitors the DC-bus voltage and determines the appropriate power-flow direction of the converter. There are four voltage levels that are relevant: reference voltage for charging, V_{chg}, reference voltage for discharging, V_{dischg}, and two transfer (threshold) voltages, $V_{transferH}$, $V_{transferL}$. These voltage levels define three operation zones, as shown in Fig. 6, in green, red, and blue lines.

As long as $v_{m1} > V_{transferH}$ the operation is always charging, with reference v_{m2}^* at the LV port. When V_{dc} drops below the first threshold, while the controller monitors the DC voltage gradient dv_{m1}/dt and if it exceeds the discharging limit $\frac{dv_{m1}}{dt} < m_{dischg} < 0$, the converter changes from charge to discharge. As long as the DC voltage is below the second threshold, $V_{m1} < V_{transferL}$, the operation is always in discharge mode with reference $v_{m1}^* = V_{m1L}$.

The transition to charging is designed with a different mechanism. When the DC microgrid voltage rises above the second threshold, $V_{m1} > V_{transferL}$, the AC–DC inverter begins operating in parallel with the DAB converter, but with its voltage reference set to V_{m1H}. Under these conditions, the voltage and current controller saturate to $\delta_{min} = 0$, because its reference v_{m1}^* becomes lower than V_{m1H} ($v_{m1}^* < V_{m1H}$). In this way, DAB naturally ceases power transfer from battery, allowing the inverter to regulate the microgrid dc voltage. Since the transition to charging is not time-critical, a buffer interval is incorporated to provide sufficient time for the AC grid to stabilize before the charging process is fully enabled.

In summary, when the voltage level is within the transition zone (red segments in Fig. 6 between the two thresholds), the transition instant is decided by the magnitude of the voltage gradient: if the gradient is outside the limits the transitions occur immediately; if the gradient is small the transitions occur at fixed thresholds $V_{transferH}$ and $V_{transferL}$. The direction of transitions is decided by the gradient sign: charge for positive and discharge for negative gradients. In this way, the microgrid achieves seamless and robust transitions without requiring communication, and the proposed strategy is applicable to systems comprising multiple parallel-connected DC-DC and AC-DC converters.

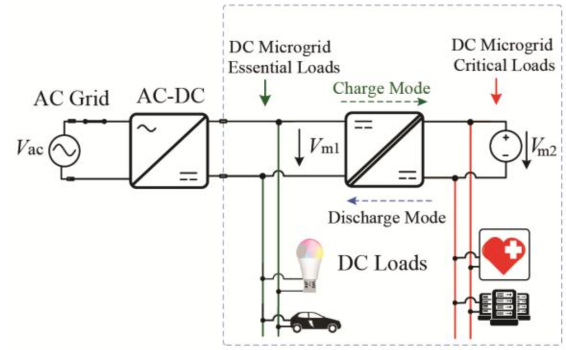

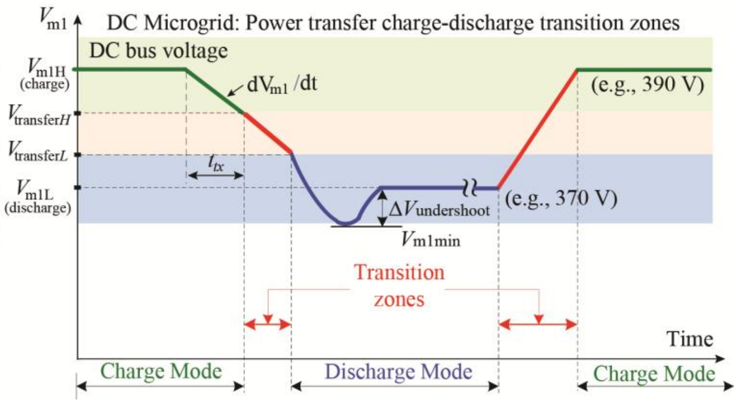

Fig. 5. Simplified Microgrid block diagram for bidirectional power flow: AC-DC inverter and DC-DC converter.

Fig. 6. Microgrid operation: proposed DC voltage gradient detection and transitions between charge and discharge modes of operations.

V. EXPERIMENTAL RESULTS

The key design parameters of the microgrid employed in the experimental tests are summarized in Table I.

TABLE I

MAIN PARAMETERS OF THE MICROGRID SYSTEM

Parameter	Symbol	Value
DC Microgrid	V_{m1}	350 ... 400 V_{dc}
Microgrid bus voltage tolerance	Δv	± % 5 V_n
DC bus voltage undershoot/overshoot	ΔV_{xv}	± % 5 V_n
AC Microgrid	V_{ac}	120/240/400 V_{ac}
Battery Voltage (DAB LV-parallel)	V_{m2}	40 ... 60 V_{dc}
Battery Voltage (DAB LV-series)	V_{m2}	80 ... 120 V_{dc}
Converter Nominal Power	P_n	6 kW
Voltage controller	K_{Pv}, K_{Iv}	0.25, 314
Current controller	K_{Pi}, K_{Ii}	0.55, 2450
Switching period	T	12μs
Phase angle gradients	$\Delta\alpha_{lim} = \Delta\beta_{lim}$	$\frac{\pi}{T}10^{-3}$

A. *Microgrid Operation in Discharge Mode.*

Fig. 7 shows the simplified microgrid block diagram for the operation in discharge mode during AC power outages.

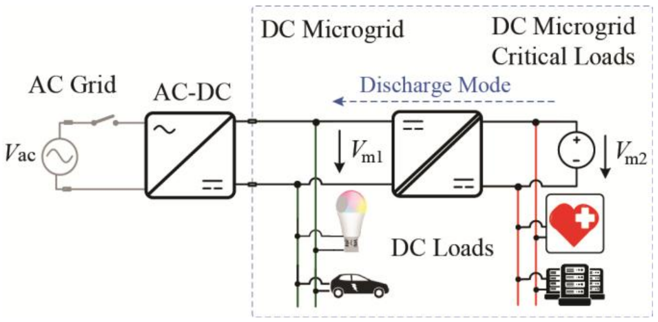

Fig. 7. Simplified block diagram of the microgrid under discharge mode testing.

Fig. 8 shows the steady-state DC-DC converter waveforms with 5 kW battery discharge from 58 V to 370 V DC microgrid bus voltage. The DC-DC converter operates with soft-switching as gate-drive signals indicate robust and noise-free time-domain waveforms.

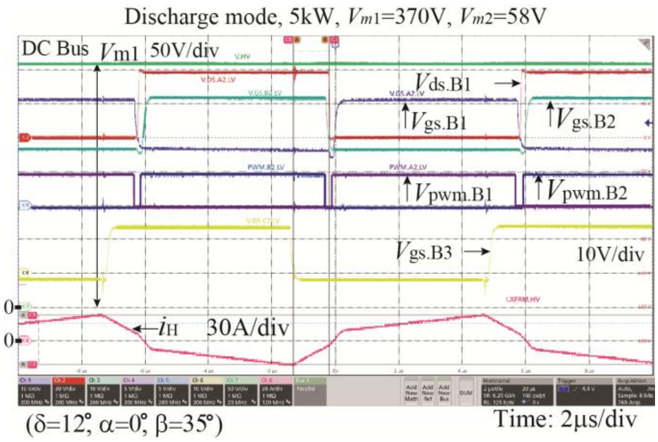

Fig. 8. DC microgrid with DAB discharge mode with experimental key waveforms in steady-state soft-switching operation.

A typical microgrid system integrates multiple power modules connected in parallel to enhance both reliability and scalability. This arrangement supports an *n+1'* redundancy scheme, ensuring that the system can maintain continuous operation even if a single module fails. Such redundancy is particularly critical for supplying uninterrupted power to essential loads, thereby improving overall system availability and fault tolerance. In this article, only one module has been considered, and Fig. 9 shows the DC-DC converter stability performance under step-load. The transformer current i_H is well balanced without concerns for transformer saturation. The test was performed with a 3.2kW step-load and the system voltage V_1 exhibited 4% undershoot (within the specification per table I) then resuming to stable microgrid operation.

B. *Microgrid Operation in Charge Mode.*

Fig. 10 shows the simplified block diagram of the microgrid operating in charge mode, where the AC-DC inverter regulates the bus voltage V_1 while the DC-DC converter controls the voltage V_2 to support critical loads and facilitate battery charging.

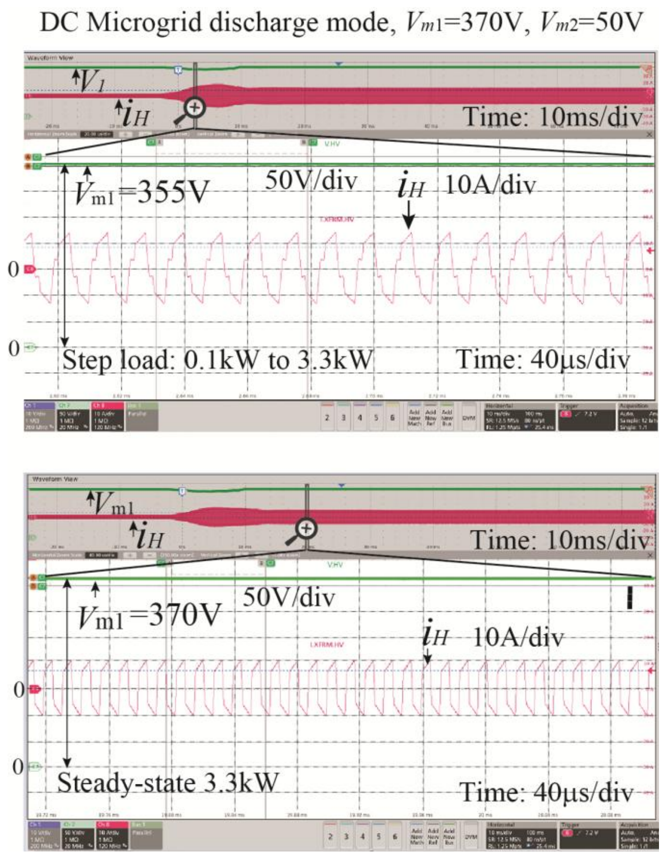

Fig. 9. DC Microgrid stability experimental test in discharge mode under step-load. Experimental results of the bidirectional DC-DC converter operating in charge mode: $V_1 = 370V, V_2 = 50V, P_1 = 0.1kW \rightarrow 3.3kW$.

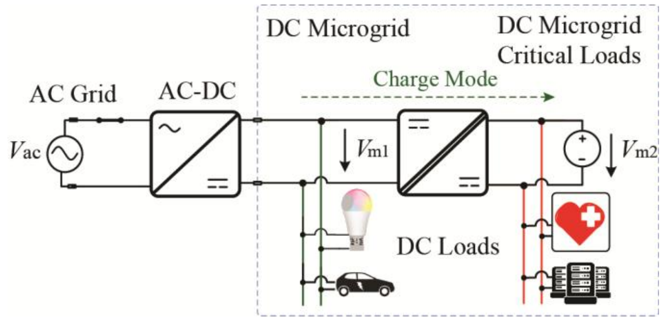

Fig. 10. Simplified block diagram of the microgrid under charge mode testing.

Fig. 10 illustrates experimental results of the DC microgrid during the start-up event. To mitigate voltage and current transients and minimize component stress, a soft-start procedure is implemented at the critical DC load port. By applying the proposed control strategy shown in Fig. 3 and Fig. 4, the bus voltage is smoothly regulated, increasing linearly from zero to the nominal 50 V level. As shown in Fig. 11, the transformer current i_H remains well balanced with its peak value effectively limited through phase-angle control. During the voltage ramp-up process, the cycle-by-cycle current control maintains a consistent current increment Δi as illustrated in Fig. 11.

This approach effectively suppresses inrush currents and eliminates adverse transient effects, resulting in a seamless and stable power transition.

C. *Microgrid Seamless Power Transfers.*

A simplified block diagram of the microgrid charge-discharge mode testing is shown in Fig. 10.

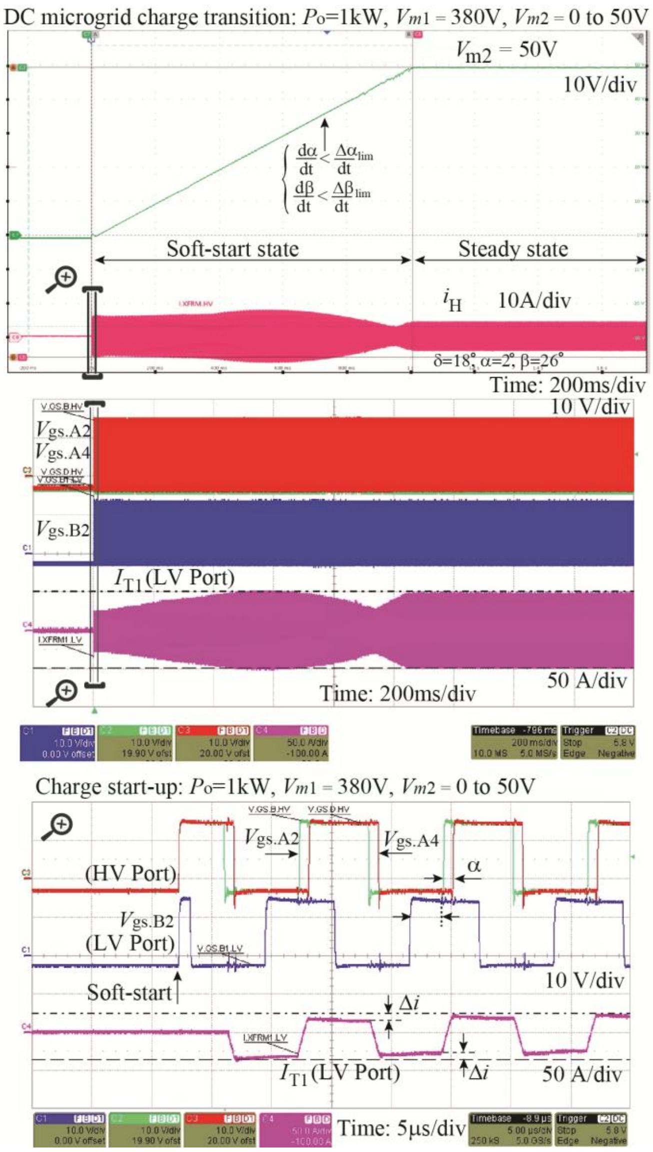

Fig. 11. Experimental results with DC microgrid start-up transition: soft-start for critical DC loads.

Under grid fault or outage conditions, the proposed microgrid architecture is tested for continuous power delivery to both general DC loads and critical loads.

Fig. 12 shows experimental results of the proposed control scheme (Fig. 3) for the DC-DC converter, operating at around 4.5kW power during dynamic state transitions. During the period of t_0 - $t_1$the DC-DC converter operates in discharge mode, regulating the dc bus at $V_{m1} = 370\ V$ where the AC-DC converter (Fig. 1) operates in grid-support for power export to the grid loads.

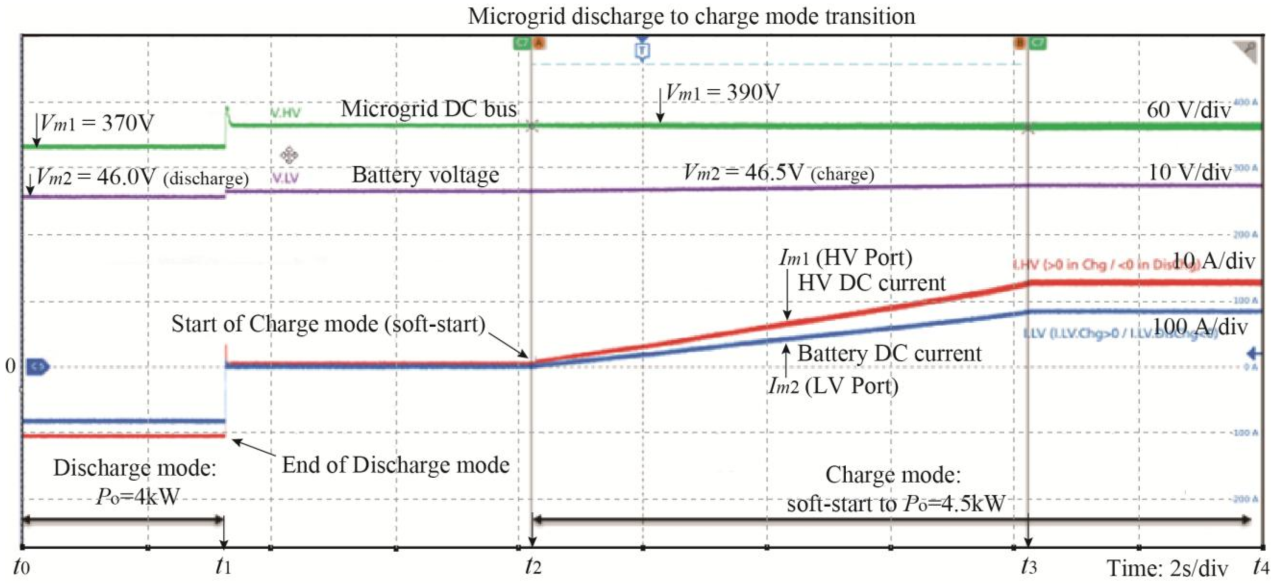

Fig. 12. Microgrid seamless transfer: bidirectional converter discharge to charge mode.

At t_1 the DC-DC converter detects a rapid dc bus increase, at the point where the AC-DC inverter regulates the dc bus at $V_{m1} = 390\ V$ corresponding to the end of discharge. A buffer interval $t_1 - t_2$ (approximatively 5 seconds) is introduced to allow sufficient time for the grid to stabilize and to prevent false detections or unnecessary transitions. At t_2 the DC-DC converter enters in battery charge mode with a soft-start and power increases to 4.5 kW at the moment t_3. The soft-start, facilitated by the controls via the triple phase-shift modulator (Fig. 3), generates a voltage ramp, minimizing the initial transient current and keeping it well within acceptable limits. During t_3 - t_4 the DC-DC converter operates in state-state for the battery charge. The transition from discharge to charge demonstrates seamless microgrid transfer operation using the proposed control strategy

Fig. 13 illustrates the performance of the proposed control scheme (Fig. 3) for fast automatic transfer from charge to discharge mode. The transition time is critical, since in the use case of AC grid outage, the response of the system must support without interruption the AC loads. During t_0 - t_1 the DC bus is regulated at $V_{m1} = 390\ V$ by the grid-connected AC-DC inverter. The DC-DC converter operates in charge mode at 50 V and 100 A for battery energy storage. At t_1 the DC bus starts to drop due to the ac grid failure and AC-DC inverter is not able to regulate the DC bus. The proposed control (Fig. 3) detects the voltage drop and between t_1 and t_2 the DC-DC converter transfers to discharge mode. The battery is discharged with 100 A in order to support the DC bus at $V_{m1} = 370\ V$. In this operating mode, the AC-DC inverter can further support the AC load demand in grid-forming mode, per Fig 1.

Upon restoration of the AC grid, the AC-DC inverter qualifies the grid voltage and frequency. In this scenario, the AC loads are supplied by the grid, and the DC bus is regulated by the AC-DC inverter to maintain $V_{m1} = 390\ V$, as per Fig. 13.

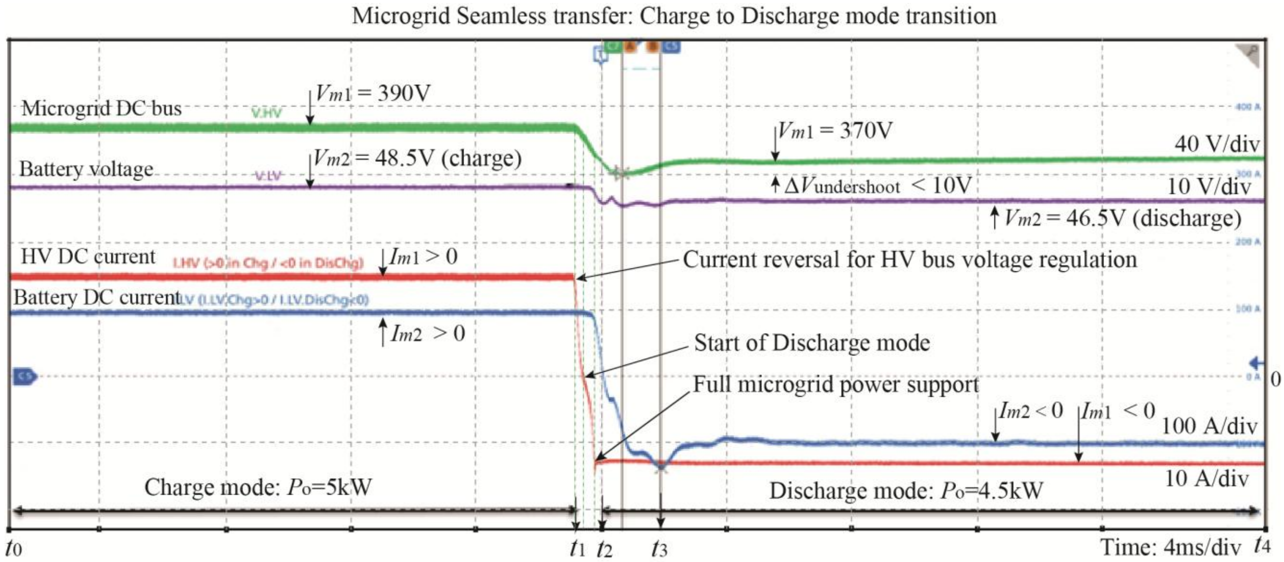

Fig. 13. Microgrid seamless transfer: bidirectional converter operation using the dc bus voltage detection for automatic transfer: charge to discharge.

The DC-DC converter demonstrates effective V_{m2} voltage regulation at the DC microgrid bus port and stable operation under full rated power conditions. The seamless transfer has been validated in both charge-discharge scenarios using the control strategy outlined in this work (Fig. 1, Fig. 3).

VI. Conclusion

This paper has presented a hybrid microgrid architecture and associated control strategy designed to ensure uninterrupted power supply to critical loads under all operating conditions. By integrating a DC uninterruptible power supply (DC-UPS), the system achieves rapid and seamless transitions between grid-connected and islanded modes. The control methodology is enhanced with a DC bus gradient detection technique, which improves detection speed for fast and automatic charge-discharge power transfer. The modulator and control were designed with symmetrical on-time and off-time balancing through the adjustment of the switching frequency. This modulator was designed to automatically execute a phase adjustment as smooth, linear slope compensation to the desired new phase while keeping the on-off time balanced.

Experimental results under both steady-state and dynamic charge-discharge conditions confirm the effectiveness of the proposed modulation and control strategies.

In summary, the work demonstrates a microgrid architecture capable of seamless power transfer within a hybrid power conversion system, with a control strategy that ensures fast power outage detection and uninterrupted power delivery to critical microgrid loads.

References

[1] M. Ahmed, L. Meegahapola, A. Vahidnia and M. Datta, "Stability and Control Aspects of Microgrid Architectures–A Comprehensive Review," in *IEEE Access*, vol. 8, pp. 144730-144766, 2020.

[2] M. Hussen and T. Rajaram, "A Comprehensive Review of Voltage Source Converters-Based FACTS Controllers in Hybrid Microgrids," in *IEEE Access*, vol. 13, pp. 62961-62999, 2025.

[3] E. Serban, C. Pondiche, H. Serban, C. Lascu and O. Cornea, "DC Voltage Control Architecture in Renewable Energy Based Three-Level Converters," 2019 IEEE Applied Power Electronics Conference and Exposition (APEC), Anaheim, CA, USA, 2019, pp. 1949-1956.

[4] E. Serban, F. Paz and M. Ordonez, "Improved PV Inverter Operating Range Using a Miniboost," in IEEE Transactions on Power Electronics, vol. 32, no. 11, pp. 8470-8485, Nov. 2017.

[5] M. E. T. Souza and L. C. G. Freitas, "Grid-Connected and Seamless Transition Modes for Microgrids: An Overview of Control Methods, Operation Elements, and General Requirements," in *IEEE Access*, vol. 10, pp. 97802-97834, 2022.

[6] H. Zhang *et al*., "A Seamless Switching Strategy for Hybrid AC/DC Microgrids Under Varied Control Complexities," in *IEEE Access*, vol. 13, pp. 122420-122431, 2025.

[7] G. Wang, X. Wang and X. Gao, "Improved Seamless Switching Control Strategy for AC/DC Hybrid Microgrid," in *IEEE Access*, vol. 9, pp. 55790-55801, 2021.

[8] E. L. Carvalho, A. Blinov, A. Chub, P. Emiliani, G. de Carne and D. Vinnikov, "Grid Integration of DC Buildings: Standards, Requirements and Power Converter Topologies," in *IEEE Open Journal of Power Electronics*, vol. 3, pp. 798-823, 2022.

[9] M. Nabatirad, R. Razzaghi and B. Bahrani, "Decentralized Voltage Regulation and Energy Management of Integrated DC Microgrids Into AC Power Systems," in *IEEE Journal of Emerging and Selected Topics in Power Electronics*, vol. 9, no. 2, pp. 1269-1279, April 2021.

[10] D. Li and C. N. M. Ho, "Decentralized PV–BES Coordination Control With Improved Dynamic Performance for Islanded Plug-n-Play DC Microgrid," in *IEEE Journal of Emerging and Selected Topics in Power Electronics*, vol. 9, no. 4, pp. 4992-5001, Aug. 2021.

[11] T. A. Fagundes, G. H. F. Fuzato, C. R. De Aguiar, K. D. A. Ottoboni, M. Biczkowski and R. Q. Machado, "Management and Equalization of Energy Storage Devices for DC Microgrids Using a SoC-Sharing Function," in *IEEE Access*, vol. 8, pp. 78576-78589, 2020.

DAB

[12] E. Serban, C. Pondiche and M. Ordonez, "Analysis and Design of Bidirectional Parallel-Series DAB-Based Converter," in *IEEE Transactions on Power Electronics*, vol. 38, no. 8, pp. 10370-10382, Aug. 2023.

[13] E. Serban, C. -M. Ancuti and C. Lascu, "Modulation Design and Control for Bidirectional Converters in Energy Storage Applications," *2025 International Aegean Conference on Electrical Machines and Power Electronics (ACEMP) & 2025 International Conference on Optimization of Electrical and Electronic Equipment (OPTIM)*, Timisoara, Romania, 2025.

[14] N. Hou and Y. Li, "Communication-Free Power Management Strategy for the Multiple DAB-Based Energy Storage System in Islanded DC Microgrid," in *IEEE Transactions on Power Electronics*, vol. 36, no. 4, pp. 4828-4838, April 2021.

[15] H. Pan, P. Cheng, H. Zhao, J. Huo, L. Jia and Q. Li, "Power Regulation of Islanded PV-Battery DC Microgrid With Seamless Transition," in *IEEE Transactions on Industry Applications*, vol. 60, no. 1, pp. 1151-1159, Jan.-Feb. 2024.

[16] X. Li, W. Jiang, J. Wang, P. Wang and X. Wu, "An Autonomous Control Scheme of Global Smooth Transitions for Bidirectional DC-DC Converter in DC Microgrid," in *IEEE Transactions on Energy Conversion*, vol. 36, no. 2, pp. 950-960, June 2021.

[17] Y. Xia, W. Wei, Y. Peng, P. Yang and M. Yu, "Decentralized Coordination Control for Parallel Bidirectional Power Converters in a Grid-Connected DC Microgrid," in *IEEE Transactions on Smart Grid*, vol. 9, no. 6, pp. 6850-6861, Nov. 2018.

[18] G. Liu, T. Caldognetto, P. Mattavelli and P. Magnone, "Power-Based Droop Control in DC Microgrids Enabling Seamless Disconnection From Upstream Grids," in *IEEE Transactions on Power Electronics*, vol. 34, no. 3, pp. 2039-2051, March 2019.

[19] B. Liu, P. Davari, and F. Blaabjerg, "An enhanced generalized average modeling of dual active bridge converters," in *2020* IEEE *Applied Power Electronics Conf. APEC*, March 2020.

[20] E.R. Diaz, F.D. Freijedo, J.C. Vasquez, and J.M. Guerrero, "Analysis and comparison of notch filter and capacitor voltage feedforward active damping techniques for LCL grid-connected converters," *IEEE Trans. Power Electron.*, vol. 34, no. 4, pp. 3958–3972, Apr. 2019.

[21] Cristian Lascu, "Sliding-mode direct-voltage control of voltage source converters with LC filters for pulsed power loads", in *IEEE Trans. Industrial Electronics*, vol. 68, no. 12, pp. 11642-11650, Dec. 2021.

[22] M. Fatu, C. Lascu, G.D. Andreescu, R. Teodorescu, F. Blaabjerg, I. Boldea, Voltage sags ride-trough of motion sensorless controlled PMSG for wind turbines, in *2007 42nd IEEE IAS Annual Meeting Conf.*, vol. 1, pp. 171-178.

[23] I. Vechiu, O. Curea and H. Camblong, "Transient Operation of a Four-Leg Inverter for Autonomous Applications With Unbalanced Load," in IEEE Transactions on Power Electronics, vol. 25, no. 2, pp. 399-407, Feb. 2010.

[24] F. Rojas et al., "An Overview of Four-Leg Converters: Topologies, Modulations, Control and Applications," in IEEE Access, vol. 10, pp. 61277-61325, 2022.